

Supplementary Material: Magnetic hysteresis of individual Janus particles with hemispherical exchange biased caps

S. Philipp,¹ B. Gross,¹ M. Reginka,² M. Merkel,² M. M. Claus,¹ M. Sulliger,¹ A. Ehresmann,² and M. Poggio¹

¹*Department of Physics, University of Basel, 4056 Basel, Switzerland*

²*Institute of Physics, University of Kassel, 34132 Kassel, Germany*

(*Electronic mail: martino.poggio@unibas.ch)

I. CANTILEVER PROPERTIES AND SIMULATION DETAILS

Cantilevers are fabricated from undoped Si. They are 75 μm -long, 3.5 μm -wide, 0.1 μm -thick with a mass-loaded end and have a 11 μm -wide paddle for optical position detection. The resonance frequency f_0 of the fundamental mechanical mode used for magnetometry is on the scale of a few kilohertz. Spring constant k_0 and effective length l_e are determined using a finite element approximation¹. For the cantilever used for the fmJP we find $f_0 = 5285.8\text{Hz}$, $k_0 = 249\mu\text{N/m}$ and $l_e = 75.9\mu\text{m}$. For the cantilever of the ebJP $f_0 = 5739.3\text{Hz}$, $k_0 = 240\mu\text{N/m}$ and $l_e = 75.9\mu\text{m}$.

Micromagnetic simulations are performed with the finite-element software package Nmag². As an approximated geometry for the JPs a semi-sphere shell with a thickness gradient from the pole towards the equator is used, that is truncated at the equator, as discussed in the main text. The exchange constant is set to $A_{ex} = 30\text{pJ/m}^3$.

In case of the fmJP, opposing to the SEM image in Fig. 2 (a) in the main text, which suggests a truncation of the fm layer by about 250 nm, it needs to be set to 350 nm or even more to match the high field progression of $\Delta f(H)$. For the same reason the nominal thickness of 10 nm of the fm layer needs to be increased to at least 12 nm at the pole, which is then gradually reduced to 0 at the equator. These two geometric constraints are necessary to keep M_s at a reasonable value below the bulk value of 1.95 MA/m⁴. This suggests, that significantly more fm material than anticipated is deposited on the region around the pole of the JPs, which is the most directly exposed area of the sphere during deposition.

For the simulation of the fmJP we set the following parameters: saturation magnetization $M_s = 1.8\text{MA/m}$, silica sphere diameter of 1.5 μm , truncation $d = 350\text{nm}$, particle orientation $(\theta_{JP}, \varphi_{JP}) = (91^\circ, 2^\circ)$ and maximum allowed mesh cell size 7.5 nm.

For the ebJP, the geometric parameters have to be adjusted less from their nominal values than for the fmJP, in order to match between the micromagnetic model to the experiment. This result suggests that the afm layer, which is deposited before the fm, acts as an adhesive for the fm, and the ebJP is coated more homogeneously than the fmJP.

For the simulation of the ebJP we set the following parameters: $M_s = 1.44\text{MA/m}$, fm layer thickness of 10 nm at the pole, gradually reduced to 0 at the equator, silica sphere diameter of 1.5 μm , $d = 350\text{nm}$, $(\theta_{JP}, \varphi_{JP}) = (85^\circ, 10^\circ)$, maximum allowed mesh cell size 7.0 nm, $(\theta_{eb}, \varphi_{eb}) = (-90^\circ, 0^\circ)$, unidirectional anisotropy constant $K_{eb} = 22.5\text{kJ/m}^3$.

For the generic simulations in sections V and IV we have used $M_s = 1.8\text{MA/m}$, fm layer thickness of 10 nm at the pole, gradually reduced to 1 nm at the equator, a silica sphere diameter of 500 nm, $(\theta_{JP}, \varphi_{JP}) = (0^\circ, 0^\circ)$, and $(\theta_{eb}, \varphi_{eb}) = (-90^\circ, 0^\circ)$. Parameters that are not mentioned here are given in the main text.

II. PROGRESSION OF THE MAGNETIC STATE WITH EXTERNAL FIELD

A. Ferromagnetic Janus particles

$\Delta f(H)$, measured for \mathbf{H} parallel to the magnetic easy (blue data) and hard axis (orange data), respectively, as shown in Fig. S1 (a), gives direct information on high field behavior and magnetic reversal of the JPs. For \mathbf{H} parallel to the magnetic easy axis, an overall V-shape suggest Stoner-Wohlfarth (SW) like behavior for most of the field range in Fig. S1 (a). As seen in the close-up in Fig. S1 (b), magnetic reversal appears to take place through a few sequential switching events at small negative reverse fields.

The simulated $\Delta f(H)$, also shown in Fig. S1 (green points) together with a few exemplary configurations of the simulated magnetic state of the JP, can give more insight into what happens during the field sweep. Starting from full saturation, most magnetic moments stay aligned with the easy direction down to very low reverse fields, nicely seen in Fig. S1, configuration 1 at 3.5 T and configuration 2 at remanence. The latter is an onion state. This progression of configurations is consistent with the Stoner-Wohlfarth-like behavior of the experimental $\Delta f(H)$. Magnetic reversal takes place through the occurrence of a so-called S-state, for which the magnetization follows the curvature of an S. The reversal is shown in configurations 3 and 4 in Fig. S1. Then, until full saturation is reached in reverse field, only magnetic moments in proximity to the equator of the JP are slightly canted away from the direction of the external field (and the easy plane). This progression is robust in simulation, even though sometimes, depending on slight variations of simulation parameters, a vortex appears in reverse field instead of the S-state. The observation of several, individual switching events during magnetic reversal in experiment may originate in vortex hopping, or switching of different regions in the JP due to variations in material and geometric parameters. Magnetic reversal through a vortex rather than an S-state may also explain the big difference of the coercive fields between experiment ($H_c \approx 32\text{mT}$) and simulation ($H_c = 6\text{mT}$).

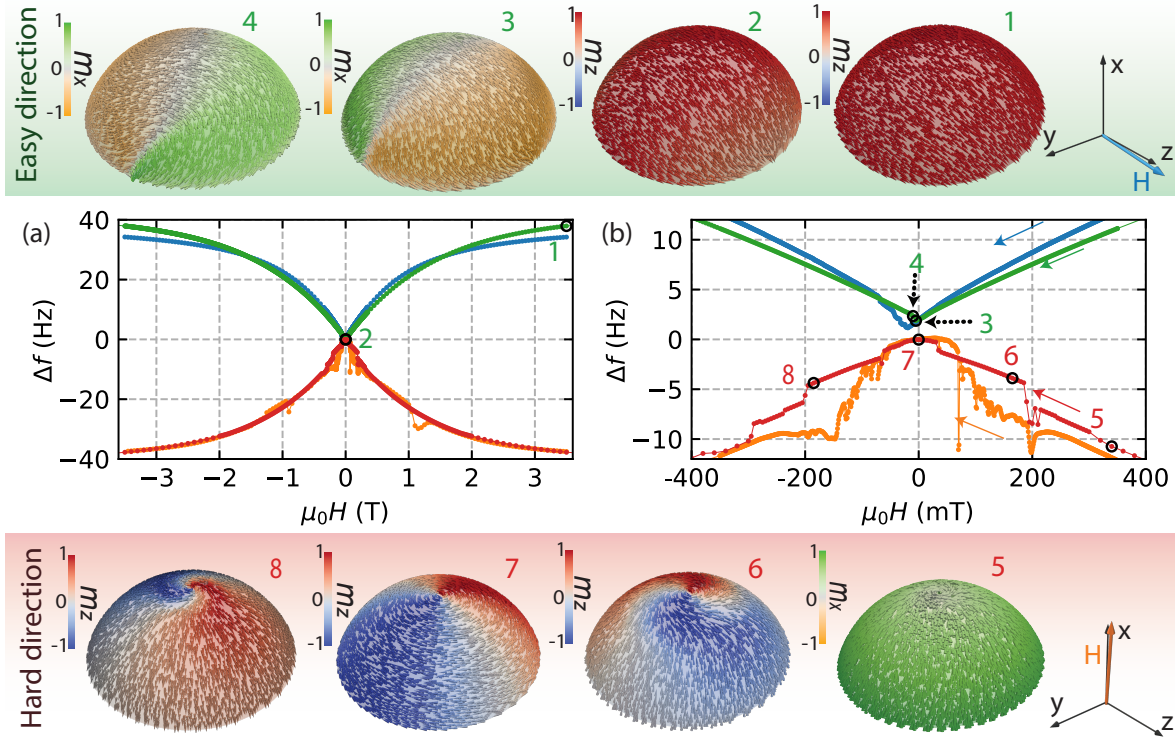


Figure S1. Data for the ferromagnetic Janus particle. (a) Measured $\Delta f(H)$ for easy (blue) and hard (orange) alignment of the external field, as well as the simulated magnetic configurations in green (easy) and red (hard). (b) Close-up of (a) for low fields. Data with easy orientation is offset by 2 Hz for better visibility. Colored arrows indicate field sweep directions. Numbers in (a) and (b) denote the field values for the configurations of the magnetic state.

For \mathbf{H} parallel to the magnetic hard axis, the experimental data has an inverted V-shape, and there is no easily identifiable sign of magnetic reversal. Yet, for relatively large fields, around 1.5 T, switching events are observed, and exist up to negative fields of similar magnitude. Typically, W-shaped curves are observed for measurements with the field aligned with the hard direction, and can be understood in a simple Stoner-Wohlfarth model, which is discussed in section III. The inverted V-shape instead of the W-shape is a peculiarity of the fact that the fm layer of the JP is curved everywhere. The angle between the local surface normal and the direction of the external magnetic field is different for every polar coordinate of the JP, which leads to a dependence of the local demagnetizing field on the polar coordinate. In consequence, the magnitude of the external magnetic field, for which the local magnetic moments start to rotate towards their local easy direction depends strongly on the position in the magnetic cap. This leads to the observed curve shape of $\Delta f(H)$, a more detailed discussion can be found in section IV. The magnetic progression in simulation for external field alignment with the hard direction can be summarized as follows: Starting from full saturation, the magnetic moments start rotating towards the easy plane with decreasing field magnitude due to the competition between shape anisotropy and Zeeman energy. This takes place for different magnitudes of \mathbf{H} depending on where a magnetic moment is located in the JP, as discussed earlier. Configuration 5 in Fig. S1 shows a state for which

magnetic moments at the pole have already started to rotate, while magnetic moments in proximity to the equator remain aligned with the external field. Superimposed to this rotation, a minimization of the system's energy by formation of a magnetic vortex localized at the pole for around 1.8 T takes place, which grows in size with decreasing field, see configuration 6. In simulation, this is a gradual evolution, and only for fields below about 300 mT jumps in Δf due to vortex movement are observed. This process is in contrast to the discontinuities that occur at around 1.5 T in the experiment, but can be explained by vortex hopping from pinning site to pinning site. The latter may be present due to fabrication inhomogeneities in the JPs⁵. For zero field the vortex dominates the magnetic configuration of the JP and has evolved into a global vortex state, as shown in configuration 7. Configuration 8 shows the vortex in reverse field, which has changed polarity, and has jumped to a slightly off-centered position. The latter is too small to be visible in the figure. Further decreasing the field, the vortex sits centrally in the JP and shrinks in size, and vanishes around -1.82 T. At the same time, the magnetic moments rotate towards the field direction depending on their position in the JP, as described earlier. Note, that by slightly changing simulation parameters, we find that features due to vortex entrance and hopping may manifest themselves in $\Delta f(H)$ with strongly differing magnitude and for different field values. Introducing artificial pinning sites in simulation can be used to adjust the vortex hopping to match the observed signals more precisely⁵,

but consumes vast amounts of computational time and should still be understood only as an exemplary progression of the magnetic state.

B. Exchange-biased Janus particles

The progression of the magnetic state for the ebJP is very similar to the fmJP, yet, there are crucial differences. See Fig. S2 for the DCM data, simulation results, and configurations of some magnetic states. For the field oriented in the magnetic easy direction the nearly polarized state, shown in Fig. S2 configuration 1, is similar to that shown in Fig. S1, configuration 1. Reducing the field down to remanence, as shown in Fig. S2 configuration 2, we find an onion state just as for the fmJP. Magnetic reversal occurs again through an S-state, rather than via vortex formation, as shown in configuration 3. However, the reversal is shifted towards negative fields, and occurs for -15 mT for the down sweep, and for -17.5 mT for the up sweep of the magnetic field. This does not match the experimentally observed values, especially for the latter case, for which the switching occurs for positive field. This is no surprise, since the employed model does not account for the contribution of the exchange bias to the coercivity. Yet, both simulation and experiment show a shift of the hysteresis loop towards negative fields as compared to the fmJP.

We only observe a single switching event in experiment for the magnetic reversal, which is consistent with the behavior of the S-state in simulation. For the alternative magnetic reversal process through vortex formation, we would expect several switching events due to vortex hopping. We find such a situation e.g. for a few reversal processes without unidirectional anisotropy, where geometrical parameters of the JPs have been varied, see section V. Yet, it is also possible, that a strong pinning site favors the formation of a vortex, and keeps it in place for all field magnitudes up to the reversal point.

If the magnetic field is swept from negative saturation up to remanence (not shown here), an onion state is present, that has its total magnetic moment pointing opposite to the exchange bias direction. For applications, this is an undesirable state. It is energetically less favorable than the state of parallel alignment, and if the energy barrier between the two states is overcome by an external influence, the JP will switch.

If the external field is aligned with the hard direction, and starts at full saturation, the magnetic moments rotate towards the easy plane depending on their position in the JP for decreasing field just as for the fmJP. Further, the same, superimposed vortex formation takes place, starting for 1.34 T. Again the vortex occupies more and more volume of the JP with further decreasing field.

Superimposed, a local vortex forms at the pole of the ebJP for an applied field of 1.34 T. As for the fmJP, the vortex occupies more and more volume of the JP with further decreasing field. However, upon further reducing the field, the vortex, rather than inhabiting the whole JP as a global vortex centered

at the pole of the fmJP, it prefers to move to the side of the ebJP, as shown in configuration 4 of Fig. S2. Moving down from the pole towards the equator, the vortex exits from the JP through the equator for 5 mT, and an onion state is formed at remanence, as shown in configuration 5. The orientation of the onion state is governed by $\hat{\mathbf{u}}_{eb}$. For a small reverse field a domain wall state forms, as shown in configuration 6. With further decreasing field, the domain wall is rotated with respect to the polar axis of the JP. This state seems to be a precursor of the vortex state, and the wall is subsequently replaced by the vortex, sitting again in the center of the JP, as shown in configuration 7. The vortex vanishes for -1.36 T. Whether such a domain wall state is indeed realized in the ebJPs for reverse fields, or if a vortex enters from the equator and moves back to the center of the JP, as seen for simulations of smaller JPs (see section V), remains an open question. The DCM signal shows in both experiment and simulation many irregularities for the lower field range, which does not allow us to draw clear conclusions on the magnetic state present in the JPs. Nevertheless, the simulations clearly suggest that an onion state should be realized at remanence, irrespective of the states present during the hysteresis. This situation is markedly different than that of the fmJP and is a direct consequence of the presence of exchange bias.

III. STONER-WOHLFARTH MODEL FOR EASY PLANE TYPE ANISOTROPY

The shape of the magnetic material of the fmJPs is, at least in a first approximation, rotationally symmetric around the pole axis. Further, the thickness gradient of the CoFe layer, as shown in the cross-sectional SEM in Fig. 1 (b) in the main manuscript, suggest that the magnetic material is concentrated in proximity to the pole, and that there is less material towards the equator. This material distribution suggests that a uniaxial anisotropy of easy plane type is imposed on the sample by its shape.

The most basic approach to describe such a system is a Stoner-Wohlfarth model, in which a single macro magnetic moment replaces the ensemble of distributed magnetic moments⁶. Following Ref. 7, it is straight forward to calculate the magnetic hysteresis and connected DCM response for easy plane anisotropy, where the latter is manifested in a positive, effective demagnetizing factor D_u , opposing to a negative D_u for easy axis anisotropy. The model is a good approximation for high fields, where all magnetic moments are aligned with the external field, and essentially behave like a single macro spin. At lower fields deviations from the curve of the SW-model indicate inhomogeneous spin orientation. We show the magnetic hysteresis of the components m_x , m_y and m_z of the normalized magnetization \mathbf{m} and the DCM response Δf in Fig. S3 for several different orientations (θ_u, ϕ_u) of the uniaxial anisotropy axis $\hat{\mathbf{u}}$, which is perpendicular to the easy plane. The external field \mathbf{H} has to be fixed in the z -direction in the model for technical reasons, which is why $\hat{\mathbf{u}}$ is varied rather than \mathbf{H} , contrary to the situation in experiment. Hence, the angles $\theta_{JP} - \theta_h$ and ϕ_{JP} , describing the equivalent situation in

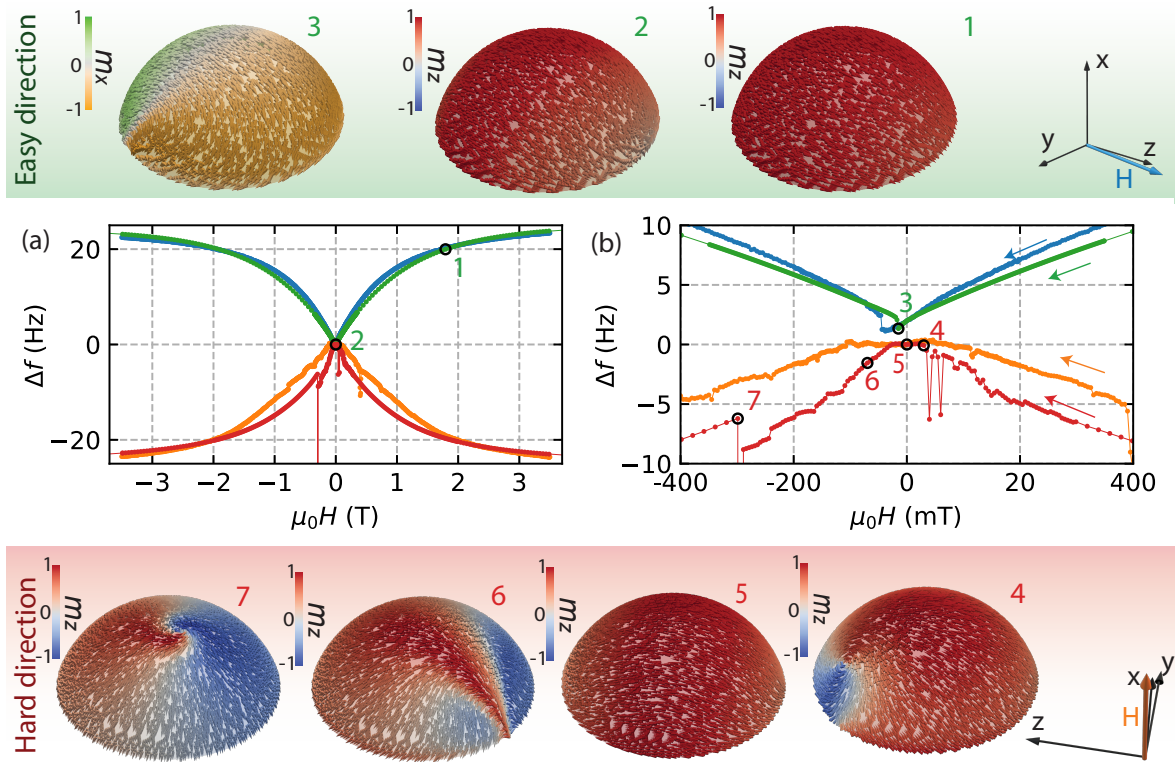


Figure S2. Data for the exchange biased Janus particle. (a) Measured $\Delta f(H)$ for easy (blue) and hard (orange) alignment of the external field, as well as the simulated pendants in green (easy) and red (hard). (b) Close-up of (a) for low fields. Data with easy orientation is offset by 2 Hz for better visibility. Numbers in (a) and (b) indicate the field values for the configurations of the magnetic state shown in (c) for hard and in (d) for easy alignment.

experiment, have to be compared to θ_u and ϕ_u , respectively. However, this does not limit the validity of the model.

For $\theta_u = 0^\circ$, for which \mathbf{H} is perpendicular to the easy plane, we find the typical W-shape for Δf for a magnetic hard orientation of \mathbf{H} ⁷. The columnar arrangement of the components of the magnetization m_x , m_y and m_z together with Δf allow to correlate changes in magnetic behavior with features in Δf , such as e.g. the transition from field alignment to the beginning of a rotation of \mathbf{m} towards the easy axis.

For $\theta_u = 90^\circ$, for which \mathbf{H} lies in the easy plane, the typical V-shaped curve for an easy orientation of \mathbf{H} is found, just as expected⁷. This V-shape is connected to \mathbf{m} perfectly aligned with \mathbf{H} . Intermediate values of θ_u lead to intermediate curve progression between the W- and V-shape. Note that magnetic reversal always takes place as soon as H crosses zero for easy plane anisotropy⁶ in the SW approximation see the arrows in Fig. S3. In experiment, it is to expect that the perfect symmetry of an easy plane anisotropy is broken, leading to a preferred axis within the plane and thus magnetic hysteresis.

Compared to experiment (see Figs. 2 and 3 in the main manuscript) we find, that while in the case of the external field \mathbf{H} in the easy plane (last panel in the last row in Fig. S3) the model generates relatively similar curve shapes for Δf , this is not true for \mathbf{H} perpendicular to the easy plane (first panel in the last row). The vertical asymptotes for $h \approx \pm 0.5$ are missing in experiment. Further, the horizontal asymptote at high field is

approached from negative rather than positive values, as it is seen in experiment. A more detailed analysis in the following section will show, that the latter originates in the curvature of the magnetic shell, which cannot be captured by a single spin model. Even though typically a good starting point, the SW model seems to be of rather limited validity for the description of the relatively specific geometry of a spherical cap.

IV. SHAPE ANISOTROPY OF A TRUNCATED SPHERICAL HALFSHELL

As a measure for the strength of the shape anisotropy present in the JPs, and as a parameter used for SW-modeling, the knowledge of the effective demagnetization factor D_u of the geometry is of value. If possible, D_u is determined using an analytical expression⁸, which, however, is not known for the given geometry. Using micromagnetic simulations as discussed in the main text, we can extract a good approximation to the demagnetization factor of a given geometry, without necessity for an analytical formula. Here, we analyze a generic, truncated spherical halfshell as defined in section I for different degrees of truncation d .

We quickly recall the definition of the effective demagnetization factor $D_u = D_z - D_x$, where D_z and $D_y = D_x$ are the demagnetization factors of a magnetic object that is rotationally

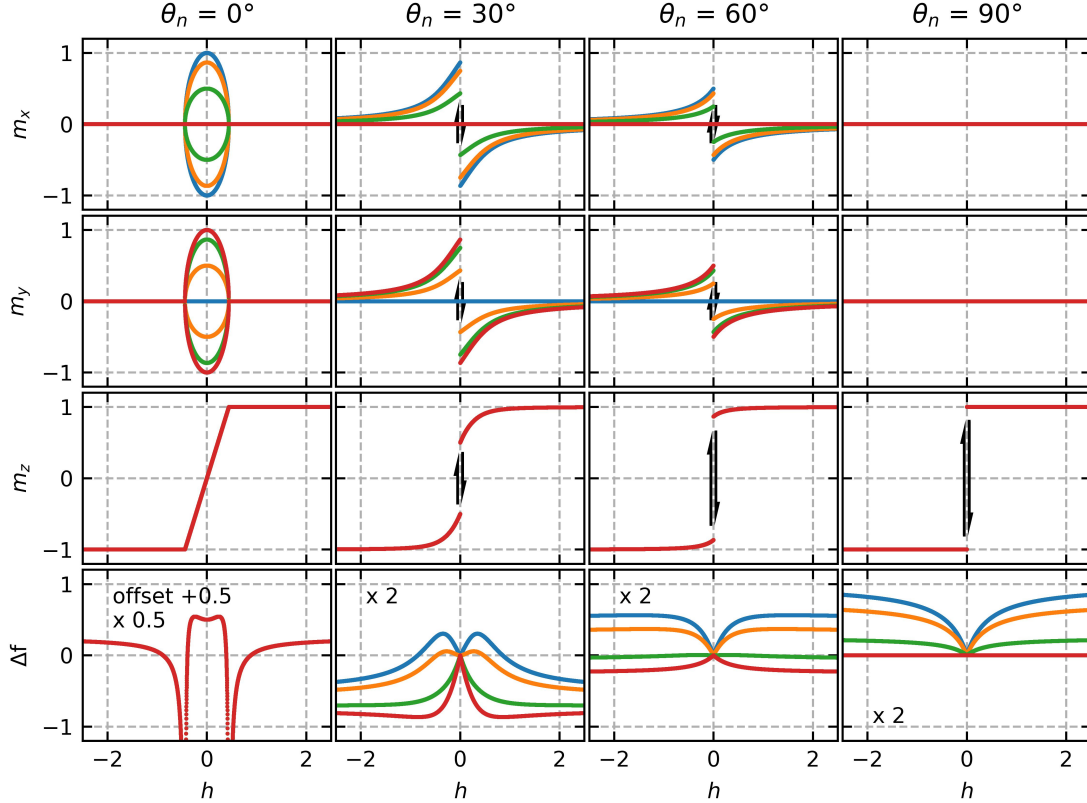


Figure S3. Components of \mathbf{M} normalized by M_s (first 3 rows) and Δf normalized by $\frac{f_0 \mu_0 V M_s^2}{2k_0 l_z^2}$ (last row) vs. normalized magnetic field $h = \frac{H}{M_s D_u}$ for different orientations of the anisotropy axis. Valid for uniaxial anisotropy with $D_u > 0$ (here $D_u = 0.5$). θ_u is increased from 0° in the first column by 30° per column up to 90° . ϕ_u is changed in the same steps, given by the different, color-coded graphs within each column (blue for $\phi_u = 0^\circ$, orange for 30° , green for 60° and red for 90°). Arrows indicate switching of the magnetization. Δf has been scaled by a factor 0.5 and offset by 0.5 for $\theta_u = 0^\circ$, and scaled by 2 for the other values of θ_u .

symmetric in the xy plane. $-0.5 < D_u < 1$ is true, and $D_u < 0$ is valid for prolate and $D_u > 0$ for oblate bodies. $D_u = 0$ is the case for a perfectly spherical body. We find a minimum D_u of approximately 0.25 for the smallest truncation, and D_u increases with truncation as shown in Fig. S4 (a). Hence, shape anisotropy gets stronger as d is increased, which can be roughly understood as the transformation from a spherical halfshell to a disc. Note, that a spherical halfshell without thickness gradient and without truncation leads to a D_u just slightly large than zero. This implies, that pointing in the easy plane is not very much more favorable than any other direction for the magnetization averaged over the whole sample, see the orange dots in Fig. S4.

The high field frequency shift, Δf_{hf} , which is of relevance for extracting anisotropy constants from experiment^{7,9}, first increases with truncation, but later decreases again, see Fig. S4 (c). This is owed to the loss of magnetic material for increasing truncation as seen in Fig. S4 (b).

In contrast to the SW model the micromagnetic simulations are able to correctly reproduce the experimental curve shape

of Δf for the hard axis orientation, see Fig. S6 (d). To understand the reason for this, the x component of the demagnetizing field $H_{demag,x}$ within the magnetic layer is visualized for a cut through the geometry in Fig. S5 at high applied field in x direction. It shows a gradual change of the demagnetizing field magnitude with z position, which is a good measure of the preferred orientation of a magnetic moment (top part with $H_{demag,x} \approx 0$ prefers x orientation, opposing to bottom part with maximum $H_{demag,x}$, which needs maximum external field to be aligned in x direction). This shows, that magnetic moments in proximity to the pole need the smallest field magnitude to be aligned with a field in x direction. The required field magnitude gradually increases the closer a magnetic moment is situated to the equator. This explains the gradual change of Δf with increasing field in this orientation, opposing to what is evident in the SW model, where all magnetic moments rotate in unison.

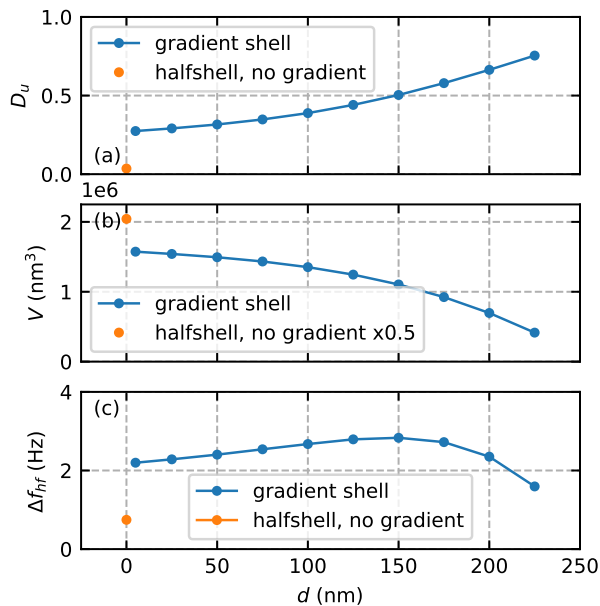


Figure S4. (a) Effective demagnetization factor D_u of a truncated spherical halfshell with a gradient shell thickness in dependence of the truncation d (blue) and of a full halfshell (orange). (b) Volume and (c) high field frequency shift Δf_{hf} of the same geometries as in (a).

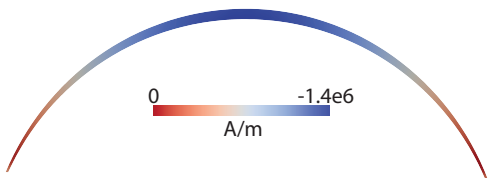


Figure S5. Cut through the geometry of the JP at the position of the xz plane showing the x component of the magnetizing field within the magnetic layer for $\mathbf{H} \parallel \hat{\mathbf{x}}$ and $\mu_0 H = 20$ T.

V. GENERIC SIMULATIONS OF TRUNCATED SPHERICAL HALFSHELLS WITH AND WITHOUT EXCHANGE BIAS

The speedup of simulations due to a reduced size of the JPs, as defined in section I, allows us to analyze the influence of simulation parameters such as the truncation on the magnetic hysteresis. In Fig. S6 a set of data for JPs with different truncations is shown. Besides the differences in high field asymptotes as already discussed in section IV, the truncation also significantly changes the curvature of $\Delta f(H)$, see Figs. S6 (a) and (d). By adjusting the truncation, this allows to fit the curvature of a given experimental $\Delta f(H)$ in the simulation.

The magnetic state evolves very much as discussed in section II for field alignment in both easy ($\mathbf{H} \parallel \hat{\mathbf{x}}$) and hard ($\mathbf{H} \parallel \hat{\mathbf{z}}$) orientation. Yet, especially for the former we observe some distinct differences for a truncation of $d > 100$ nm: Rather than through the formation of an S-state close to remanence, magnetic reversal occurs through a vortex state, that only ap-

pears for small reverse fields. This manifests itself e.g. in the magnitude of the total magnetic moment $|\mu|$, which is significantly less for the vortex state as compared to the S-state, as shown in Fig. S6 (b).

For the external magnetic field perpendicular to the easy plane, we find that magnetic reversal takes place via vortex formation for all values of the truncation. Consequently, the total magnetic moment at remanence is always small, as seen in Figs. S6 (b) and (e).

There is a big difference between the magnetic moments at remanence depending on through which progression remanence has been reached. Hence, in order to find the most stable state, it is instructive to compare the energies of the different progressions as shown in Figs. S6 (c) and (f). A state with significant $|\mu|$ at remanence always seems to possess higher energy than the vortex state. Compare, for example, the energy at remanence for the JP with 200 nm truncation for easy (no vortex) and hard (vortex state) field alignment. The former has about 40 aJ, while the latter is more favorable with only 7 aJ.

As discussed in the main text, exchange bias, which forces magnetic moments into a certain direction, can avoid a global vortex state at remanence. We simulate the magnetic hysteresis of reduced-size JPs with global unidirectional anisotropy and vary its strength K_{eb} . As an example, we pick a JP with a cut of 100 nm, and match the orientation of the unidirectional anisotropy to the parallel field direction, which gives the maximum effect in the DCM signal.

In Fig. S7, we plot the same set of data for the JP with exchange bias as for the purely ferromagnetic JPs in Fig. S6. The frequency shift for high fields for $\mathbf{H} \parallel \hat{\mathbf{x}}$ develops an increasing asymmetry for increasing strength K_u of the unidirectional anisotropy, as shown in Fig. S7 (a). In turn, for perpendicular alignment this asymmetry is not evident, as shown in Fig. S7 (d). Hence, the experimentally observed asymmetry in the asymptotes can serve as good indicator for the strength of the unidirectional anisotropy, given that its orientation is known. The main influence of the unidirectional anisotropy on the progression of the magnetic state with external field for easy field alignment is to shift magnetic reversal in magnetic field magnitude. This can e.g. be seen in $|\mu|$, see Fig. S7 (b). Magnetic reversal takes place around zero field for $K_{eb} = 1 \text{ kJ/m}^3$, and is shifted to happen around 50 mT for $K_{eb} = 100 \text{ kJ/m}^3$. The dominant state during reversal remains an onion state for all values of K_{eb} . For hard alignment, a vortex appears in the JP for all values of K_{eb} , just as described in section II B. The vortex is centered in the JP for larger field magnitudes, but moves to the side of the JP, if the field is reduced. Depending on K_{eb} , the vortex moves only very little (small values for K_{eb}), moves significantly to the side of the JP (intermediate K_{eb}), or even escapes the JP through the equatorial line (large values of K_{eb}). If the latter happens, the vortex reenters the JP in reverse field from the other side of the JP and then moves back to the center for increasing reverse field. The larger the K_{eb} , the larger is the total magnetic moment μ at remanence, for $K_{eb} = 100 \text{ kJ/m}^3$ we find almost full saturation in direction of the anisotropy vector, see Fig. S7 (e).

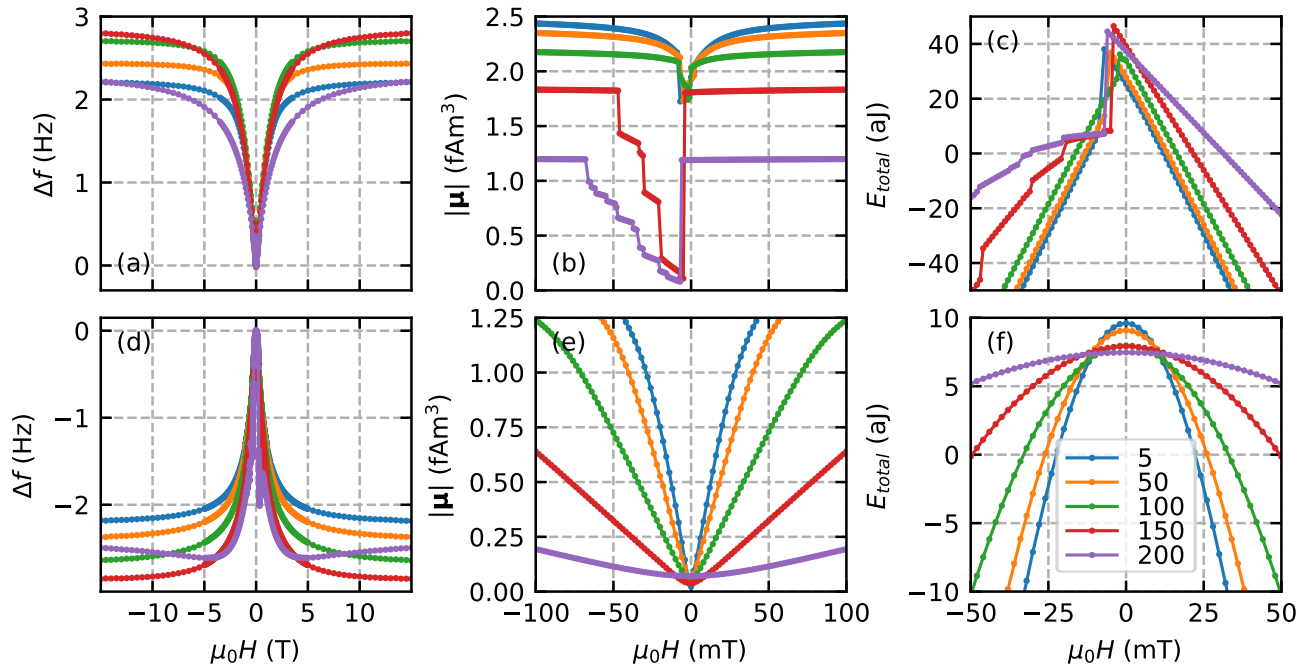


Figure S6. Frequency shift Δf , total magnetic moment μ and total energy E_{total} for JPs with different truncation as indicated in the legend in nm. Top row: External field applied in the easy plane ($\mathbf{H} \parallel \hat{x}$). Bottom row: External field applied in the hard direction ($\mathbf{H} \parallel \hat{z}$).

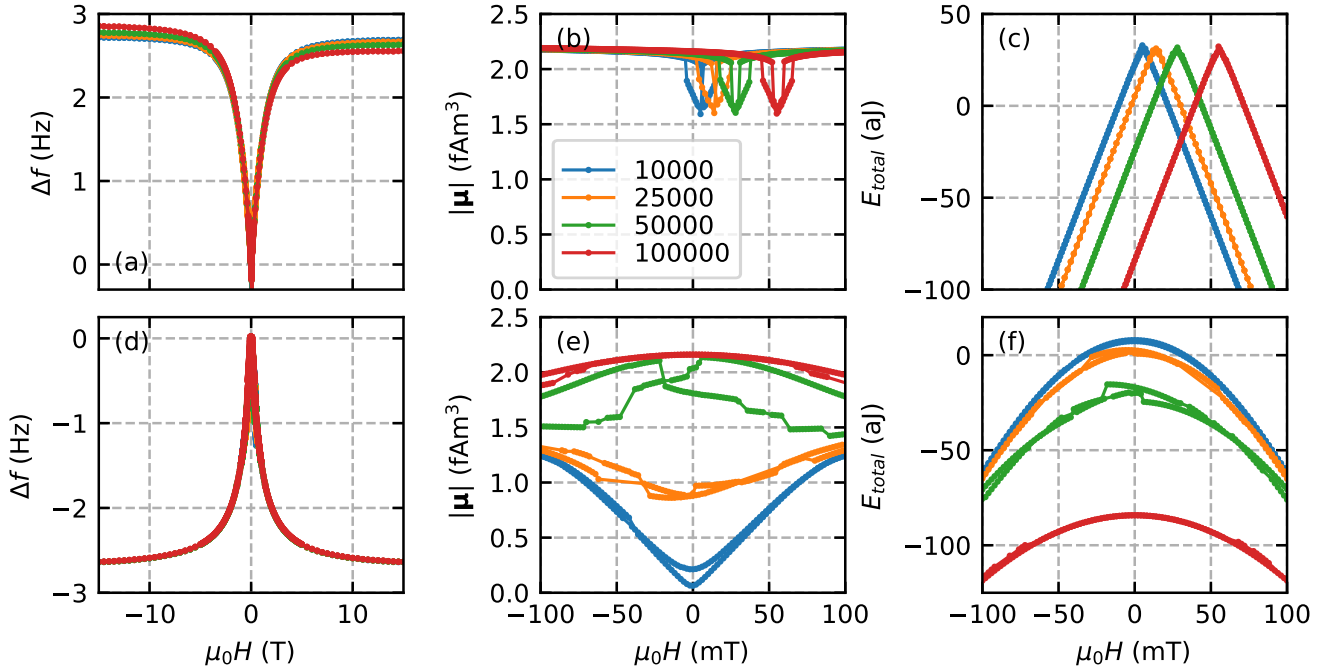


Figure S7. Frequency shift Δf , total magnetic moment μ and total energy E_{total} for JPs with 100 nm truncation and different strengths of the unidirectional anisotropy as indicated in the legend in J/m³. Top row: External field applied in the easy plane ($\mathbf{H} \parallel \hat{x}$). Bottom row: External field applied in the hard direction ($\mathbf{H} \parallel \hat{z}$).

A clear trend is observable, if we consider the energy that sets which remanent state is more likely over long time scales, as shown in Figs. S7 (c) and (f): The difference in energy between the remanent states gets smaller for increasing K_{eb} , and hence diminishes the relevance of the chosen orientation

of an applied field to magnetize the JP. The trend for the total magnetic moment is, irrespective of the which orientation for the external field is chosen, to be larger in magnitude if K_{eb} is increased.

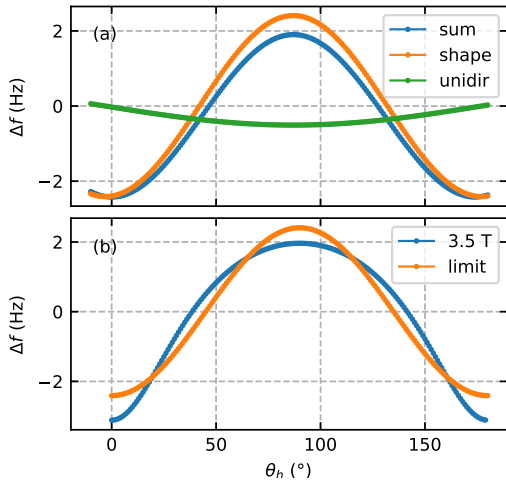


Figure S8. (a) $\Delta f(\theta_h)$ in the high field limit with shape and unidirectional anisotropy. $\Delta f(\theta_h)$ in the SW model for 3.5 T applied field magnitude, and in the high field limit from (a).

VI. DCM IN THE HIGH-FIELD LIMIT WITH UNIDIRECTIONAL ANISOTROPY

The high-field limit in DCM is reached for $|H| \gg |\sum_i K_i / (\mu_0 M_s)|$, where K_i are the different anisotropy contributions for a given direction. The frequency shift of the cantilever resonance is determined in this limit by the competition of the different anisotropy contributions, and can be calculated analytically^{7,9}. For the presence of unidirectional anisotropy of strength K_{eb} this is given by:

$$\Delta f_{\text{unidir}} = -\frac{f_0 V K_{eb}}{2k_0 l_e^2} \left(\begin{aligned} & \cos \theta_u (\sin \theta_h \sin \theta_{eb} \cos \phi_u \cos \phi_{eb} + \cos \theta_h \cos \theta_{eb}) \\ & - \sin \theta_{eb} (\sin \theta_u \cos \theta_h \cos \phi_{eb} + \sin \theta_h \sin \phi_u \sin \phi_{eb}) \\ & + \sin \theta_u \sin \theta_h \cos \theta_{eb} \cos \phi_u \end{aligned} \right) \quad (\text{S1})$$

Here, $(\theta_h, \phi_h = 0)$ define the orientation of the external field, (θ_u, ϕ_u) of the axis of the uniaxial shape anisotropy as defined in Ref. 9, and (θ_{eb}, ϕ_{eb}) of the unidirectional anisotropy vector. The latter is oriented first, and rotated by (θ_u, ϕ_u) in a second step to be consistent with the situation in experiment. Cantilever and magnetic parameters are as defined before.

We evaluate the high-field limit for the sum of shape and unidirectional anisotropy for an exemplary situation as it may be present for the exchange biased JPs, using similar parameters as in section IV. However, we increase K_{eb} significantly to magnify its effects. The angles are set to be $(\theta_u, \phi_u) = (-3^\circ, 0^\circ)$ and $(\theta_{eb}, \phi_{eb}) = (-90^\circ, 0^\circ)$, while θ_h is varied as in experiment. The result is shown in Fig. S8 (a), to-

gether with the individual contributions from shape and unidirectional anisotropy. This shows, that the sum of the two contributions may lead to a periodicity that deviates slightly from 180° , which would be given for pure uniaxial shape anisotropy. Furthermore, the magnitude of maxima and minima may differ significantly. Here we find 1.9 Hz for the maxima and 2.4 Hz for the minima, respectively. We have indeed observed such large asymmetries in experiment for low temperatures (not shown here), however, the origin is different, as will be discussed in the following. Nevertheless, for strong unidirectional anisotropies these findings should be observable in experiment.

The SW model, as described in section III, can be used to calculate $\Delta f(\theta_h)$ for a fixed field magnitude, as done in experiment for 3.5 T. This allows to compare the result of the SW model with the high field limit as discussed above, see Fig. S8 (b). The curve of the high field limit follows a (negative) cosine with $2\theta_h$ in the argument. In turn, for the SW model at 3.5 T, minima are deeper and maxima are shallower in Δf , respectively. However, there is no deviation from the 180° periodicity. Further, maxima are wider than minima, which is a consequence of the fact that positive and negative asymptotes are approached with a different curvature when ramping up the external field in the SW model, compare curves in the last panel in the first column with those in the last panel in the last column in Fig. S3. In experiment this behavior of the maxima and minima is inverted, which is caused by the extreme curvature of the magnetic layer JPs, as discussed in section IV.

REFERENCES

- ¹COMSOL AB. Comsol multiphysics®, 2021.
- ²T. Fischbacher, M. Franchin, G. Bordignon, and H. Fangohr. A systematic approach to multiphysics extensions of finite-element-based micromagnetic simulations: Nmag. *IEEE Transactions on Magnetics*, 43(6):2896–2898, 2007.
- ³D. V. Berkov, C. T. Boone, and I. N. Krivorotov. Micromagnetic simulations of magnetization dynamics in a nanowire induced by a spin-polarized current injected via a point contact. *Physical Review B*, 83(5):054420, February 2011. Publisher: American Physical Society.
- ⁴J. M. D. Coey. *Magnetism and Magnetic Materials*. Cambridge University Press, 2010.
- ⁵N. Rossi, B. Gross, F. Dirnberger, D. Bougeard, and M. Poggio. Magnetic force sensing using a self-assembled nanowire. *Nano Letters*, 19(2):930–936, 2019.
- ⁶Allan H. Morrish. *The Physical Principles of Magnetism*. Wiley, January 2001.
- ⁷B. Gross, D. P. Weber, D. Ruffer, A. Buchter, F. Heimbach, A. Fontcuberta i Morral, D. Grundler, and M. Poggio. Dynamic cantilever magnetometry of individual CoFeB nanotubes. *Phys. Rev. B*, 93(6):064409, February 2016.
- ⁸A. Hubert and R. Schäfer. *Magnetic Domains: The Analysis of Magnetic Microstructures*. 1998.
- ⁹B. Gross, S. Philipp, E. Josten, J. Leliaert, E. Wetterskog, L. Bergström, and M. Poggio. Magnetic anisotropy of individual maghemite mesocrystals. *Phys. Rev. B*, 103:014402, Jan 2021.